A&A, 712, L1 (2026)
https://doi.org/10.1051/0004-6361/202660291

Astronomy & Astrophysics

Letter to the Editor

Discovery of EP J175257.3–351923 as a candidate black hole low-mass X-ray binary

G. L. Huang[1,2], Q. C. Zhao[1,2], L. Tao[1,⋆], A. Coleiro[3], A. Rau[4], S. Brennan[4], C. Y. Dai[5,6], R. Soria[7,8], F. Cangemi[3], F. Coti Zelati[9,10], A. Marino[9,10], L. Zhang[1], S. Guillot[11], H. Q. Cheng[12], H. Feng[1], D. Götz[13], Y. Huang[1], Y. F. Huang[5,6], D. Y. Li[12], Z. S. Li[14], P. Maggi[15], R. C. Ma[16], X. Ma[1], H. W. Pan[12], N. Rea[9,10], J. Wang[12], Q. Y. Wu[12], L. P. Xin[12], W. M. Yuan[12], Z. H. Yao[12], G. B. Zhang[17], W. D. Zhang[12], and S. N. Zhang[1]

(Affiliations can be found after the references)

Received 8 April 2026 / Accepted 20 June 2026

ABSTRACT

We report the discovery of a new X-ray transient, EP J175257.3–351923 (EP250916a), by the *Einstein* Probe (EP) near the galactic plane. The outburst lasted for at least 250 days and reached a peak 2–10 keV flux of $\sim 4 \times 10^{-10}$ erg cm^{-2} s^{-1}, exhibiting a fast-rise exponential-decay (FRED) profile typical of X-ray binary outbursts. The source remained in the hard state throughout the outburst, with only modest variations in the photon index (∼1.6–2.2) and no evidence of a spectral state transition. Broadband spectral modeling suggests a truncated disk, a weak reflection component, and a high-energy cutoff at ∼217 keV, consistent with hard-state accretion in black-hole systems. No reliable optical or radio counterpart has been detected within the *Swift*/XRT error circle. The inferred X-ray-to-optical and X-ray-to-radio flux ratios are consistent with a low-mass X-ray binary (LMXB) classification. Neither pulsations nor significant aperiodic variability were detected. Although the compact object cannot yet be firmly identified, the timing, spectral, and multiwavelength evidence favors the classification of EP J175257.3–351923 as a black-hole (BH) LMXB candidate, highlighting EP's potential to uncover a faint, previously hidden population of X-ray binaries.

Key words. accretion, accretion disks – black hole physics

1. Introduction

X-ray binaries (XRBs) are binary systems composed of a compact object that is either a neutron star (NS) or a black hole (BH), along with a stellar companion. Most low-mass XRBs (LMXBs) are transient sources that remain predominantly in a quiescent state (Tanaka & Shibazaki 1996; Tetarenko et al. 2016). Episodically, these systems undergo X-ray outbursts lasting from weeks to months, likely driven by thermal-instability (Lasota 2001), typically reaching peak luminosities of $L_X \sim 10^{37}$–10^{39} erg s^{-1} (Yan & Yu 2015; Tetarenko et al. 2016; Bahramian & Degenaar 2023). The discovery of these transients has relied on a series of wide-field X-ray monitors launched since the 1970s, including Ariel-V, Granat/WATCH, RXTE/ASM, INTEGRAL, *Swift*/BAT, and MAXI (e.g., Villa et al. 1976; Brandt et al. 1990; Levine et al. 1996; Winkler et al. 2003; Barthelmy et al. 2005; Matsuoka et al. 2009). However, such monitors often miss faint XRBs (peak luminosity of $L_X \sim 10^{36-37}$ erg s^{-1}) and the extreme cases of very faint XRBs (VFXBs; $L_X \sim 10^{34-36}$ erg s^{-1}; Wijnands et al. 2006). The low luminosities of these systems most likely arise from low mass-transfer rates, due to their small accretion disks, evaporation of the inner disk into a radiatively inefficient flow, or propeller effects in the case of NS systems (Bahramian & Degenaar 2022). The launch of the *Einstein* Probe (EP; Yuan et al. 2022, 2025) has greatly advanced the sensitivity of wide-field monitoring, enabling the detection of previously elusive faint sources and thereby providing insights into the low-luminosity accretion regime that has rarely been explored thus far.

⋆ Corresponding author: taolian@ihep.ac.cn

Over its first two years of operation, EP has discovered more than a dozen faint XRB candidates, such as EP240809a (MAXI J1752–457; Liu et al. 2024 and Cheng et al., in prep.), EP240904a (EP J182730.0–095633; Cheng et al. 2025b), EP250315b (EP J163933.2–411414; Li et al. 2025 and Li et al. 2026), EP J174942.2–384834 (Coti Zelati et al. 2026), and EP250623a (EP J171159.4–333253; Wang et al. 2026 and Yang et al., in prep.). These detections demonstrate EP's unique capacity to explore the previously unexplored population of faint XRBs.

Here, we report the discovery of a new faint XRB candidate, EP J175257.3–351923 (designated EP250916a), and present results from the follow-up observations. Section 2 describes the observations and data reduction. Section 3 presents the analysis and results, followed by our discussion and conclusions in Sect. 4.

2. Observations

EP J175257.3–351923 was first detected by the Wide-field X-ray Telescope (WXT) on board EP at 03:33:13 UTC on 2025 September 16 (Fig. 1; Wu et al. 2025; Dai et al. 2025a). EP/WXT continued monitoring this source until 2025 October 17, with typical exposures of ∼1–3 ks per epoch. Following a several-month-long interruption due to Sun-avoidance constraints, monitoring resumed on 2026 March 15. Multiwavelength follow-up observations (Table D.1) were performed with the EP/Follow-up X-ray Telescope (FXT; Chen et al. 2021), Space-based multiband astronomical Variable Objects Monitor (SVOM; Wei et al. 2016; Atteia et al. 2022), *Neil Gehrels*

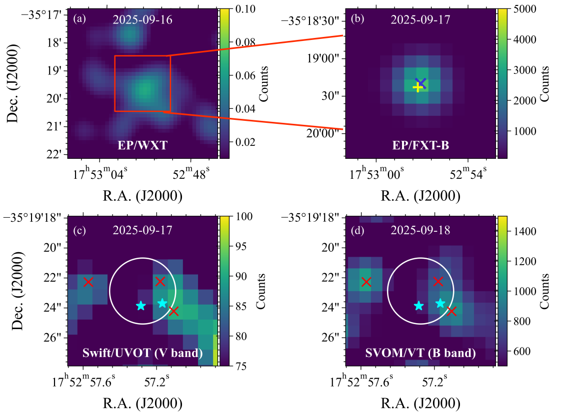

Fig. 1. Multiwavelength images of EP J175257.3–351923. (a) EP/WXT discovery image of the new transient. (b) EP/FXT-B follow-up image. The blue cross and yellow plus mark the EP/FXT and *Swift*/XRT positions, respectively. (c) *Swift*/UVOT *V*-band image. The white circle shows the *Swift*/XRT positional uncertainty (2.2″, 90%), red crosses mark three cataloged sources detected in both *Gaia* and VIRAC2/VVVX, and cyan stars indicate two additional sources listed only in VIRAC2/VVVX. (d) SVOM/VT *B*-band image, with the same symbols as in panel (c). All images have been smoothed for display purposes.

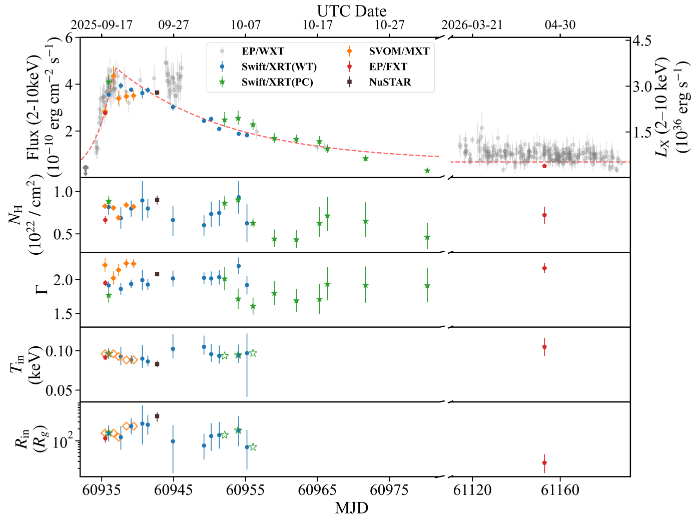

Fig. 2. Long-term X-ray evolution: unabsorbed 2–10 keV flux/luminosity, hydrogen column density ($N_{\rm H}$), power-law index (Γ), inner disk temperature ($T_{\rm in}$), and inner disk radius ($R_{\rm in}$). Open symbols indicate fixed diskbb values. Different symbols correspond to different instruments. The solid red line represents the best-fitting FRED model (excluding the pre-outburst EP/WXT upper limit). Luminosity and $R_{\rm in}$ are calculated assuming $D = 8$ kpc, $M = 10\,M_\odot$, and $i = 58^\circ$ (Table D.2).

Swift Observatory (*Swift*; Gehrels et al. 2004), Nuclear Spectroscopic Telescope Array (*NuSTAR*; Harrison et al. 2013), and Gamma-Ray burst Optical Near-infrared Detector (GROND; Greiner et al. 2008). The source region was also covered by the Very Large Array Sky Survey (VLASS; Lacy et al. 2020) on 2026 February 1.

The observation with EP/FXT (~32 h post-discovery; ~3.1 ks) detected a bright X-ray source within the EP/WXT error circle at RA (J2000) = $17^{\rm h}52^{\rm m}57.1^{\rm s}$ and Dec (J2000) = $-35^\circ19'19.9''$, with a 10″ uncertainty (90% confidence; Dai et al. 2025b). *Swift*/XRT further refined the position to RA (J2000) = $17^{\rm h}52^{\rm m}57.3^{\rm s}$ and Dec (J2000) = $-35^\circ19'22.9''$ (l = 355.3090°, b = −4.6086°), with a 2.2″ uncertainty at the 90% confidence (Illiano et al. 2025). We adopted the XRT position to search for the multiwavelength counterpart. Details of the data reduction are provided in Appendix A.

3. Analysis and results

3.1. Multiwavelength counterpart

As shown in the lower panels of Fig. 1 and in Fig. A.1, five cataloged optical/infrared sources are located within or near the *Swift*/XRT error circle. Three of these are recorded in both *Gaia* DR3 (Gaia Collaboration 2023) and VIRAC2/VVVX (Smith et al. 2025), while the remaining two are only cataloged in VIRAC2/VVVX. Photometry in this crowded field is challenging due to source confusion. We performed small-aperture photometry on the three *Gaia* sources using *Swift* Ultra-Violet/Optical Telescope (UVOT) data obtained during the outburst (see Appendix A for details). Although suboptimal, this approach allows us to examine whether the optical emission traces the X-ray variability. In contrast to the order-of-magnitude variability observed in X-rays, the optical fluxes of these sources vary by less than a factor of 1 during the outburst and show no evolutionary track comparable to that of the X-ray light curve. For the GROND data, reliable photometry is not feasible due to crowding. These sources are therefore likely chance alignments with the EP source, although a true counterpart cannot be fully excluded.

To constrain the optical emission from the EP source, we derived upper limits at the XRT position instead (see Appendix A). Aperture photometry performed at the *Swift*/XRT error circle yielded 3σ upper limits of $V > 17.77$ mag from *Swift*/UVOT (ObsID: 03000100002) on September 17 and $B > 18.71$ mag from the SVOM Visible Telescope (VT; ObsID: 06333) on September 18. We also searched the VLASS quick-look image without detecting a radio counterpart within the XRT error circle, deriving a 3σ upper limit of 4.44×10^{-4} Jy beam^{-1} at 3 GHz (Appendix A.6).

3.2. X-ray spectral analysis

The X-ray spectral analysis was performed with XSPEC v12.14.0b (Arnaud 1996) using data from EP/WXT (0.5–4.0 keV), EP/FXT (0.5–10 keV), *Swift*/XRT (0.3–10 keV), SVOM Microchannel X-ray Telescope (MXT; 0.4–10 keV), and *NuSTAR* (4–78 keV). Interstellar absorption was modeled with tbabs adopting the solar abundances of Wilms et al. (2000), and a cross-calibration constant was included in joint fits. Unabsorbed X-ray fluxes were estimated using the cflux convolution model. The details of the spectral fitting are given in Appendix B.

3.3. Long-term X-ray evolution

The long-term evolution of the flux is shown in Fig. 2. Archival EP/WXT observations performed on 2025 September 14 and 15 yield a pre-outburst unabsorbed 2–10 keV flux upper limit of $\sim 4 \times 10^{-11}$ erg cm^{-2} s^{-1}. Following the onset of the outburst at MJD 60934 (2025 September 16), the source exhibited a rapid flux increase, peaking at ~MJD 60936 (2025 September 18), after which the emission entered a gradual decay phase. The X-ray light curve is well described by a fast-rise exponential-decay

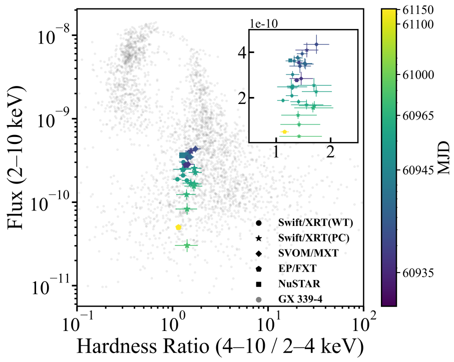

Fig. 3. HID during the outburst. EP/WXT data are excluded due to the narrow energy band. The inset shows a zoomed-in view. Faint gray points show long-term MAXI data of GX 339–4 ("q"-like tracks of "successful" outbursts are evident) for comparison.

(FRED) profile, characterized by a rise timescale of ∼2.5 days and a decay timescale of ∼15.7 days (see Appendix C.1).

The Γ remained within ∼1.6–2.2 throughout the outburst, with no clear evidence of spectral softening. To further investigate the state evolution during the outburst, we constructed a hardness–intensity diagram (HID; Fig. 3). Hardness is defined as the ratio of unabsorbed fluxes in the 4–10 keV and 2–4 keV bands, and intensity as the unabsorbed flux in the 2–10 keV band. The HID indicates that the source remained in the hard state, with no evidence of a state transition.

The N_H ranges from 4×10^{21} to 9×10^{21} cm^{-2} during the outburst, showing no significant evolution within the uncertainties. The N_H values exceed the Galactic HI column density of $\sim 2 \times 10^{21}$ cm^{-2} from the HI4PI survey (HI4PI Collaboration 2016)[1], hinting at potential intrinsic absorption. However, given the uncertainties in the HI4PI Galactic estimate, this apparent excess may instead stem from differential reddening in the Galactic bulge.

3.4. Timing analysis

We inspected all available X-ray light curves and found no evidence of Type-I bursts. Average power spectral densities (PSDs) were computed using stingray v2.3.2 (Huppenkothen et al. 2019; Bachetti et al. 2024), based on 512 s segments from 0.005 s barycenter-corrected light curves of EP/FXT-B, *Swift*/XRT (WT mode), SVOM/MXT, and *NuSTAR*. No significant coherent pulsations, quasi-periodic oscillations (QPOs), or red noise were detected, whereas the higher signal-to-noise *XMM-Newton* observation revealed a weak QPO at a frequency of ∼13 Hz (Jaisawal et al. 2026). The averaged power spectra (fractional-rms normalization; Fig. D.2) from *NuSTAR* gave a 99% upper limit of 10.3% on the integrated rms over 0.1–64 Hz. An acceleration search using PRESTO (Ransom 2011) found no significant pulsations, implying a 99% upper limit of ∼6–7% on the pulsed fraction.

4. Discussion and conclusions

We report the discovery of a new long-duration X-ray transient, EP J175257.3–351923, located at a Galactic latitude of $b = -4.6086°$, close to the Galactic plane where the space density of XRBs reaches its maximum (Grimm et al. 2002; Bahramian & Degenaar 2023). The source exhibits characteristics analogous to those of XRBs. Its long-term X-ray light curve exhibits a characteristic FRED morphology, a hallmark of transient XRB outbursts (Chen et al. 1997; Remillard & McClintock 2006). The outburst persists for at least ∼250 days, well within the typical duration range observed in Galactic XRB transients (Tetarenko et al. 2016; Heinke et al. 2025). The source maintains a remarkable spectral stability throughout the outburst, remaining in the hard state with only limited variation in photon index. Such behavior is commonly referred to as a "failed outburst" and has been reported in hard-state outbursts of XRBs (Tetarenko et al. 2016; Yan & Yu 2015). Furthermore, broadband spectral modeling suggests a truncated accretion disk together with a reflection component, with a photon index of Γ ∼ 1.6–2.2 and a high-energy cutoff at ∼217 keV, broadly consistent with the canonical hard-state characteristics of XRBs (Done et al. 2007; Bu & Zhang 2023).

No reliable optical or radio counterpart was detected within the *Swift*/XRT localization region in the available *Swift*/UVOT, SVOM/VT, GROND, and VLASS images. The optical non-detection is likely due to the combined effects of strong interstellar extinction, weak optical brightening associated with the faint X-ray outburst, and source confusion in the crowded Galactic-plane environment. The radio non-detection may also reflects weak emission from the faint outburst. Assuming a representative distance of 8 kpc and a reddening of $E(B-V) = 0.40$ mag (Wang et al. 2025), we derived a 3σ upper limit on the de-reddened B-band magnitude, $B_0 \gtrsim 18.58$ mag (using the extinction law of Cardelli et al. 1989). Using quasi-simultaneous X-ray and optical data, we derived a lower limit on the X-ray-to-optical flux ratio, defined as $\xi = B_0 + 2.5 \log F_X$, yielding $\xi \gtrsim 21.75$. This is consistent with values typically observed in LMXBs (Lewin et al. 1995). Furthermore, assuming a distance of 8 kpc, both the X-ray-to-optical and X-ray-to-radio luminosity ratios display a broad agreement with the hard-state LMXB correlations (see Figs. D.3 and D.4; Russell et al. 2006; Bahramian & Rushton 2022). Collectively, the temporal, spectral, and multiwavelength properties favor the classification of this source as a LMXB candidate, which is consistent with the findings of Jaisawal et al. (2026).

EP J175257.3–351923, with an X-ray luminosity of the order of $\sim 10^{36}$ erg s^{-1}, can be classified as a faint or VFXB candidate according to Wijnands et al. (2006). In particular, in many VFXBs the companions are expected to be intrinsically faint (e.g., low-mass main-sequence stars). The multiwavelength correlations observed for EP J175257.3–351923 are consistent with this scenario. Moreover, the long-term light-curve morphology, and photon-index evolution of this EP source resemble those of VFXBs such as EP J182730.0–095633 (Cheng et al. 2025b) and IGR J17285−2922 (Stoop et al. 2021), both of which have been proposed as BH candidates. Interestingly, a stable QPO at ∼40 mHz with a fractional rms amplitude of ∼20–30% has been detected in EP J182730.0–095633. In contrast, we do not detect any significant QPO in EP J175257.3–351923; the PSD is largely featureless. Nevertheless, featureless PSDs have also been reported in several VFXBs (Koch et al. 2014; van den Eijnden et al. 2018; Marino et al. 2022). Furthermore, the presence of a truncated accretion disk and a reflection component is in good agreement with the properties reported for the VFXBs IGR J17062–6143 and MAXI J1848–015 (van den Eijnden et al. 2018; Pike et al. 2022).

Based on the FRED modeling, the decay timescale of ∼15.7 days implies an outer disk radius of $\sim 10^4 R_g$ (Appendix C.2). Assuming this radius is comparable to the circularization radius, we derived an estimated orbital period of

[1] https://heasarc.gsfc.nasa.gov/cgi-bin/Tools/w3nh/w3nh.pl

~4.3 h. Although these estimates are subject to considerable uncertainties arising from both the model assumptions and the choice of system parameters, this source is likely a short-period system with a relatively small accretion disk. An analogous example is Swift J1357.2−0933, a short-period ($P \approx 3$ h) BH XRB transient in the VFXB regime (Mata Sánchez et al. 2015). Such short-period systems represent a proposed channel for the formation of VFXBs (Heinke et al. 2015).

Regarding the nature of the compact object, the absence of coherent pulsations, Type-I X-ray bursts, and dynamical mass measurements leaves both NS and BH interpretations viable. However, the high cut-off energy of ~217 keV inferred from spectral modeling favors a BH system (Burke et al. 2017). This is because seed photons from an NS surface and boundary layer enhance Compton cooling, generally leading to lower cut-off energies, whereas the absence of a solid surface in BHs allows for deeper gravitational energy release and higher electron temperatures (Burke et al. 2017; Pszota 2024).

Aside from an XRB classification, alternative interpretations such as a classical nova or a tidal disruption event (TDE) appear less likely. Classical novae are typically associated with prominent supersoft X-ray emission (Chomiuk et al. 2021), which is absent in this source. Thermal TDEs generally exhibit soft X-ray spectra (Mummery et al. 2023), whereas the X-ray spectrum of this EP source remains persistently hard. Moreover, unlike jetted TDEs such as Swift J1644+57 (Mimica et al. 2015) and AT2022cmc (Rhodes et al. 2023), which display bright radio emission detectable for months to years, no radio counterpart is found in the VLASS images at the position of this source, further disfavoring the TDE interpretation.

Overall, future multiwavelength observations, particularly with large-aperture optical telescopes, will be essential to further constrain the nature of the compact object and to fully characterize the physical properties of this system. Nevertheless, this source provides an interesting case for understanding weak outbursts, while demonstrating EP's capacity to discover faint XRBs.

Acknowledgements. We thank the anonymous referee for comments that helped improve the paper. This work made use of data from EP, SVOM, *NuSTAR*, and *Swift*. This work was supported by the National Key R&D Program of China (Nos. 2025YFF0511102 and 2021YFA0718500), the National Natural Science Foundation of China (Nos. 12122306, 12025301, and 12103027), the Strategic Priority Research Program of the Chinese Academy of Sciences, and China's Space Origins Exploration Program. SG acknowledges the support of the CNES. F.C.Z. is supported by the Ramón y Cajal fellowship (RYC2021-030888-I), Spanish grant ID2023-153099NA-I00, and the program Unidad de Excelencia Maria de Maeztu CEX2020-001058-M. Part of the funding for GROND (both hardware and personnel) was generously granted by the Leibniz-Prize to G. Hasinger (DFG grant HA 1850/28-1) and by the Thüringer Landessternwarte Tautenburg. Y. F. H. also acknowledges the support from the Xinjiang Tianchi Program.

References

Arnaud, K. A. 1996, ASP Conf. Ser., 101, 17
Atteia, J.-L., Cordier, B., & Wei, J. 2022, Int. J. Mod. Phys. D, 31, 2230008
Bachetti, M., Huppenkothen, D., Stevens, A., et al. 2024, J. Open Source Softw., 9, 7389
Bahramian, A., & Degenaar, N. 2022, in Low-Mass X-ray Binaries, eds. C. Bambi, & A. Santangelo (Singapore: Springer Nature Singapore), 1
Bahramian, A., & Degenaar, N. 2023, in Handbook of X-ray and Gamma-ray Astrophysics, 120
Bahramian, A., & Rushton, A. 2022, https://doi.org/10.5281/zenodo.7059313
Barthelmy, S. D., Barbier, L. M., Cummings, J. R., et al. 2005, Space Sci. Rev., 120, 143
Blanton, M. R., & Roweis, S. 2007, AJ, 133, 734
Brandt, S., Lund, N., & Rao, A. R. 1990, Adv. Space Res., 10, 239
Bu, Q., & Zhang, S. 2023, in Handbook of X-ray and Gamma-ray Astrophysics, 139
Burke, M. J., Gilfanov, M., & Sunyaev, R. 2017, MNRAS, 466, 194
Cardelli, J. A., Clayton, G. C., & Mathis, J. S. 1989, ApJ, 345, 245
Cash, W. 1979, ApJ, 228, 939
Chen, W., Shrader, C. R., & Livio, M. 1997, ApJ, 491, 312
Chen, Y., Cui, W., Han, D., et al. 2021, SPIE Conf. Ser., 11444, 114445B
Cheng, H., Zhang, C., Ling, Z., et al. 2025a, Exp. Astron., 60, 15
Cheng, H. Q., Zhao, Q. C., Tao, L., et al. 2025b, ApJ, 991, L41
Chomiuk, L., Metzger, B. D., & Shen, K. J. 2021, ARA&A, 59, 391
Coti Zelati, F., Marino, A., Wang, Y. L., et al. 2026, ApJ, 1003, 224
Dai, C. Y., Wu, Q. Y., Li, D. Y., & Pan, H. W. 2025a, ATel, 17395, 1
Dai, C. Y., Wu, Q. Y., Li, D. Y., Pan, H. W., & Einstein Probe Team 2025b, GCN, 41861, 1
Dauser, T., Garcia, J., Wilms, J., et al. 2013, MNRAS, 430, 1694
Done, C., Gierliński, M., & Kubota, A. 2007, A&ARv, 15, 1
Evans, P. A., Beardmore, A. P., Page, K. L., et al. 2009, MNRAS, 397, 1177
Frank, J., King, A., & Raine, D. 1992, Camb. Astrophys. Ser., 21
Gaia Collaboration (Vallenari, A., et al.) 2023, A&A, 674, A1
García, J., Dauser, T., Lohfink, A., et al. 2014, ApJ, 782, 76
Gehrels, N., Chincarini, G., Giommi, P., et al. 2004, ApJ, 611, 1005
Götz, D., Crepaldi, S., Doumayrou, E., et al. 2026, Res. Astron. Astrophys., in press
Greiner, J., Bornemann, W., Clemens, C., et al. 2008, PASP, 120, 405
Grimm, H. J., Gilfanov, M., & Sunyaev, R. 2002, A&A, 391, 923
Harrison, F. A., Craig, W. W., Christensen, F. E., et al. 2013, ApJ, 770, 103
Heinke, C. O., Bahramian, A., Degenaar, N., & Wijnands, R. 2015, MNRAS, 447, 3034
Heinke, C. O., Zheng, J., Maccarone, T. J., et al. 2025, ApJS, 279, 57
HI4PI Collaboration (Ben Bekhti, N., et al.) 2016, A&A, 594, A116
Huppenkothen, D., Bachetti, M., Stevens, A. L., et al. 2019, ApJ, 881, 39
Illiano, G., Zanon, A. M., Sbarufatti, B., et al. 2025, ATel, 17397, 1
Jaisawal, G. K., Illiano, G., Carotenuto, F., et al. 2026, ApJ, in press
Koch, E. W., Bahramian, A., Heinke, C. O., et al. 2014, MNRAS, 442, 372
Krühler, T., Küpcü Yoldas, A., Greiner, J., et al. 2008, ApJ, 685, 376
Lacy, M., Baum, S. A., Chandler, C. J., et al. 2020, PASP, 132, 035001
Lasota, J.-P. 2001, New Astron. Rev., 45, 449
Levine, A. M., Bradt, H., Cui, W., et al. 1996, ApJ, 469, L33
Lewin, W. H. G., van Paradijs, J., & van den Heuvel, E. P. J. 1995, in X-ray Binaries (Cambridge, MA: Cambridge University Press)
Li, D. Y., Shui, Q. C., Huang, M. Q., Liu, Y., & Yuan, W. 2025, ATel, 17083, 1
Li, P., Tao, L., Soria, R., et al. 2026, ApJ, submitted
Liu, H. Y., Yang, H. N., Li, D. Y., et al. 2024, ATel, 16765, 1
Maggi, P., Michel, L., Götz, D., et al. 2026, Res. Astron. Astrophys., in press
Marino, A., Anitra, A., Mazzola, S. M., et al. 2022, MNRAS, 515, 3838
Mata Sánchez, D., Muñoz-Darias, T., Casares, J., Corral-Santana, J. M., & Shahbaz, T. 2015, MNRAS, 454, 2199
Matsuoka, M., Kawasaki, K., Ueno, S., et al. 2009, PASJ, 61, 999
Mimica, P., Giannios, D., Metzger, B. D., & Aloy, M. A. 2015, MNRAS, 450, 2824
Mummery, A., Wevers, T., Saxton, R., & Pasham, D. 2023, MNRAS, 519, 5828
Pike, S. N., Negoro, H., Tomsick, J. A., et al. 2022, ApJ, 927, 190
Powell, C. R., Haswell, C. A., & Falanga, M. 2007, MNRAS, 374, 466
Pszota, G. 2024, Universe, 10, 446
Ransom, S. 2011, Astrophysics Source Code Library [record ascl:1107.017]
Remillard, R. A., & McClintock, J. E. 2006, ARA&A, 44, 49
Rhodes, L., Bright, J. S., Fender, R., et al. 2023, MNRAS, 521, 389
Riello, M., De Angeli, F., Evans, D. W., et al. 2021, A&A, 649, A3
Russell, D. M., Fender, R. P., Hynes, R. I., et al. 2006, MNRAS, 371, 1334
Smith, L. C., Lucas, P. W., Koposov, S. E., et al. 2025, MNRAS, 536, 3707
Stoop, M., van den Eijnden, J., Degenaar, N., et al. 2021, MNRAS, 507, 330
Tanaka, Y., & Shibazaki, N. 1996, ARA&A, 34, 607
Tetarenko, B. E., Sivakoff, G. R., Heinke, C. O., & Gladstone, J. C. 2016, ApJS, 222, 15
van den Eijnden, J., Degenaar, N., Pinto, C., et al. 2018, MNRAS, 475, 2027
Villa, G., Page, C. G., Turner, M. J. L., et al. 1976, MNRAS, 176, 609
Wang, T., Yuan, H., Chen, B., et al. 2025, ApJS, 280, 15
Wang, Y. L., Coti Zelati, F., Parent, E., et al. 2026, ApJ, 1003, 22
Wei, J., Cordier, B., Antier, S., et al. 2016, arXiv e-prints [arXiv:1610.06892]
Wijnands, R., in't Zand, J. J. M., Rupen, M., et al. 2006, A&A, 449, 1117
Wilms, J., Allen, A., & McCray, R. 2000, ApJ, 542, 914
Winkler, C., Courvoisier, T. J. L., Di Cocco, G., et al. 2003, A&A, 411, L1
Wu, Q. Y., Dai, C. Y., Li, D. Y., Pan, H. W., & Einstein Probe Team 2025, GCN, 41841, 1
Yan, Z., & Yu, W. 2015, ApJ, 805, 87
Yao, Z. H., Qiu, Y., Deng, J. S., et al. 2026, Res. Astron. Astrophys., accepted
Yuan, W., Zhang, C., Chen, Y., & Ling, Z. 2022, in Handbook of X-ray and Gamma-ray Astrophysics, eds. C. Bambi, & A. Sangangelo, 86
Yuan, W., Dai, L., Feng, H., et al. 2025, Sci. China: Phys. Mech. Astron., 68, 239501

[1] Key Laboratory of Particle Astrophysics, Institute of High Energy Physics, Chinese Academy of Sciences, Beijing 100049, PR China
[2] University of Chinese Academy of Sciences, Chinese Academy of Sciences, Beijing 100049, China
[3] Université Paris Cité, CNRS, Astroparticule et Cosmologie, F-75013 Paris, France
[4] Max Planck Institute for Extraterrestrial Physics, Garching 85748, Germany
[5] School of Astronomy and Space Science, Nanjing University, Nanjing 210023, China
[6] Key Laboratory of Modern Astronomy and Astrophysics (Nanjing University), Ministry of Education, Nanjing 210023, China
[7] INAF-Osservatorio Astrofisico di Torino, Strada Osservatorio 20, I-10025 Pino Torinese, Italy
[8] Sydney Institute for Astronomy, School of Physics A28, The University of Sydney, NSW 2006, Australia
[9] Institute of Space Sciences (ICE, CSIC), Campus UAB, Carrer de Can Magrans s/n, E-08193 Barcelona, Spain
[10] Institut d'Estudis Espacials de Catalunya (IEEC), 08860 Castelldefels (Barcelona), Spain
[11] IRAP, Université de Toulouse/OMP, CNRS, CNES, 9 avenue du Colonel Roche, BP 44346, F-31028 Toulouse Cedex 4, France
[12] National Astronomical Observatories, Chinese Academy of Sciences, Beijing 100101, China
[13] CEA Paris-Saclay, Institut de Recherche sur les lois Fondamentales de l'Univers, 9111 Gif-sur-Yvette, France
[14] School of Science, Qingdao University of Technology, Qingdao 266525, China
[15] Observatoire Astronomique de Strasbourg, Université de Strasbourg, CNRS, 11 rue de l'Université, F-67000 Strasbourg, France
[16] School of Physics and Astronomy, University of Southampton, Highfield, Southampton SO17 1BJ, UK
[17] Yunnan Observatory, Chinese Academy of Sciences, Kunming 650011, China

Appendix A: Data reduction

A.1. EP

To provide full coverage of the outburst, in addition to the follow-up observations (Table D.1), we also use survey data from EP/WXT. The WXT spectra were extracted using the standard wxtpipeline pipeline (Liu et al., in prep.) and the latest calibration database (CALDB), which is based on results from ground calibration experiments (Cheng et al. 2025a). Due to the limited photon statistics of the WXT data, the spectra were grouped to a minimum of one count per bin using grppha in HEASoft v6.34, and spectral fitting was performed using the Cash statistic (C–stat; Cash 1979).

Owing to solar angle constraints, EP/FXT observations were carried out on 2025 September 17 (upper-right panel of Fig. 1) and on 2026 April 22. For the first observation, we analyzed only the FXT module B (FXT-B) data taken in partial window (PW) mode with the fxtchain tool, as the module A (FXT-A) operating in full frame (FF) mode was affected by severe pile-up. Both PW and FF mode data were used for the second observation. Source and background spectra were extracted from a circular region with a radius of 90″ and from an annulus spanning 150″–240″ centered on the source position, respectively. The spectra were grouped to a minimum of 25 counts per bin using grppha.

A.2. NuSTAR

NuSTAR observed this source on 2025 September 24 (ObsID 91101336002; ∼ 21 ks). Data were processed with nupipeline and CALDB version 20250922. Source events were extracted from a circular region of 60″ radius centered on the source, and background events were extracted from a rectangular region free of stray light and sufficiently distant from the source. The spectra, light curves, and response files were produced using nuproducts, and the spectra were grouped to a minimum of 25 counts per bin.

A.3. Swift

Swift/XRT performed high-cadence monitoring of EP J175257.3–351923 starting on 2025 September 17 and continuing for approximately one month, with a total of 21 observations. The spectra were extracted using the online tool provided by Evans et al. (2009)[2]. For spectra with more than 1500 total counts, the data were binned to ≥ 25 counts per bin and fitted using χ^2 statistics. For spectra with fewer counts, the data were grouped to a minimum of one count per bin and fitted using Cash statistic.

The UVOT monitored the source contemporaneously with XRT. Some observations were performed only in the V band, while others included both the B and V bands. We analyzed the Level 3 data products.

For potential optical counterparts (see Sect. 3.1), aperture photometry was performed using uvotsource with a 1″ aperture and a nearby background region of 5″ radius free of sources. While this small aperture is suboptimal for absolute photometry, it was chosen to minimize contamination from the crowded stellar field. As our analysis focuses on the evolution of optical flux during the outburst for counterpart identification, uncertainties in the aperture correction do not affect the observed trends. To estimate the upper limit of the optical emission from EP J175257.3–351923, an aperture of 2.2″ (corresponding to the *Swift*/XRT localization uncertainty) and a circular background of 5″ radius were used. We note that with an aperture of 2.2″, emission from nearby sources is included, yielding an overestimated upper limit, though this does not affect the constraints on the companion type based on the X-ray-to-optical flux ratio (Sec. 4). Aperture corrections were applied using the apercorr=CURVEOFGROWTH option. All magnitudes reported in this work are given in the Vegamag system.

Aperture photometry of the three *Gaia* sources within or near the *Swift*/XRT error circle using *Swift*/UVOT data gives averaged magnitudes of V = 18.19, 18.46, and 18.16 mag over the outburst, broadly consistent with the V-band magnitudes (V = 17.70, 18.91, and 18.10 mag) derived from *Gaia* DR3 using the relation of Riello et al. (2021). However, we need to point out that the small aperture used may introduce systematic uncertainties in the magnitudes.

A.4. SVOM

SVOM conducted five follow-up observations between 2025 September 17 and 21, before the source became inaccessible owing to solar constraints. The VT data from September 17 were lost due to telemetry failures.

The MXT (Götz et al. 2026) on board SVOM observed the source during this period. The event-mode data were processed with version 1.13 of the MXT pipeline (Maggi et al. 2026). Source detection was performed via point-spread function fitting, and the pipeline was used to extract the source and background spectra, along with the associated response files, from the event lists. Owing to the relatively high background of the MXT data, the spectra were grouped to a minimum of one count per bin using grppha and analyzed with the C–stat.

The VT on board SVOM also observed the source region contemporaneously with WXT, with an exposure time of 70 s per frame. Level 2 data products, including dark and flat-field corrections, were used. Aperture photometry was performed using photutils in Python, with aperture corrections applied. The source aperture sizes and background regions adopted for nearby *Gaia* sources and for estimating the upper limit of the optical emission from EP J175257.3–351923 are identical to those used for *Swift*/UVOT. The magnitudes were first converted to the Johnson B-band AB system following Yao et al. (2026), and subsequently transformed to the Vegamag system using the relation of Blanton & Roweis (2007).

The ECLAIRs data were also examined, but the source was not detected.

A.5. GROND

This source was observed with the GROND mounted on the MPG 2.2 m telescope at ESO's La Silla Observatory. Observations were carried out simultaneously in the g', r', and i' bands, as well as in the H and K_s bands, on 2025 September 17 at 01:02 UT, September 18 at 23:55 UT, and September 27 at 01:12 UT. The total exposure times were 33 min in the optical and 30 min in the near-infrared. The data were reduced using the standard IRAF-based GROND pipeline (Krühler et al. 2008).

A.6. VLASS

The source position was covered by VLASS on 2026 February 1. No radio counterpart is detected within the XRT error circle in the VLASS quick-look image. The local rms noise

[2] https://www.swift.ac.uk/user_objects/

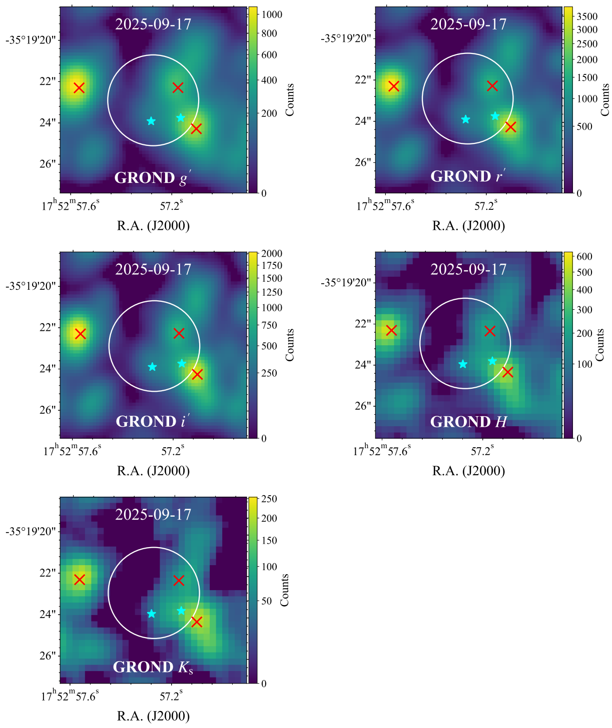

Fig. A.1. GROND observations on 2025 September 17. The images have been smoothed for display purposes. Symbols follow the same convention as in Fig. 1.

was measured within a circular region of radius 20″ centered on the XRT position, yielding a 3σ flux density upper limit of 4.44×10^{-4} Jy beam^{-1} at 3 GHz.

Appendix B: Details of X-ray spectral fitting

B.1. Swift/XRT and EP/FXT

Between 2025 September 17 and October 8, the *Swift*/XRT WT-mode spectra require an absorbed power-law plus diskbb model (simftest proves the diskbb addition is statistically significant, $p < 0.01$). For the *Swift*/XRT PC-mode spectra, the diskbb parameters could not be constrained because of limited photon statistics after excluding central pixels to mitigate pile-up. They were therefore fixed to the values derived from temporally adjacent WT-mode observations. After October 8, a single absorbed power-law is sufficient. For the two EP/FXT observations, the spectra are best fitted with an absorbed power-law plus diskbb model.

B.2. SVOM/MXT

The SVOM/MXT spectra alone do not require an additional thermal component and are adequately described by a single absorbed power-law model. For consistency with the *Swift*/XRT and EP/FXT spectral analysis, we nevertheless adopted the same absorbed power-law plus diskbb model when fitting the MXT spectra. However, when the diskbb parameters were fixed to the values derived from adjacent *Swift*/XRT observations, the inferred power-law photon index became significantly softer. This behavior indicates a degeneracy between the thermal and non-thermal components within the MXT bandpass. We caution that the MXT-derived photon index should be interpreted cautiously due to these degeneracies.

B.3. EP/WXT

For the EP/WXT spectra during the outburst, the narrow energy coverage and limited photon statistics allowed only an absorbed power-law fit, with $N_{\rm H}$ fixed to the value derived from the adjacent EP/FXT observations and Γ fixed at 2.

To derive the pre-outburst flux upper limit, we combined the three WXT observations covering this position obtained on 2025 September 14 and 15, yielding a total exposure time of $\sim$ 6400 s. The source region was defined as a circle centered on the *Swift*/XRT position with a radius of 9.2′, while the background was extracted from a nearby source-free region with a radius of 30′. The 90% upper limit on the count rate was converted to an unabsorbed flux upper limit using the count-rate-to-flux conversion factor, assuming an absorbed power-law model with $N_{\rm H}$ derived from the first EP/FXT observation and $\Gamma = 2$.

B.4. Joint NuSTAR and Swift spectral fitting

The *NuSTAR* spectra obtained on 2025 September 24 were fitted jointly with two quasi-simultaneous *Swift*/XRT observations taken on September 23 and 26 to improve soft-band photon statistics. An absorbed cutoff power-law improves the fit over a simple power-law, reducing χ^2/d.o.f. from 2158/1669 to 2093/1668, yielding a cutoff energy of 154^{+41}_{-27} keV. However, the cutoff power-law model still leaves soft X-ray residuals and a weak broad hump at 20–40 keV (Fig. D.1), suggesting the presence of additional disk and reflection components. Consequently, we used constant*tbabs*(cutoffpl+relxill+diskbb) to fit the spectra, where relxill is a model for relativistic reflection on an accretion disk (Dauser et al. 2013; García et al. 2014). As several parameters of relxill could not be well constrained, we fixed the BH spin (a) at 0.998, the inner disk radius ($R_{\rm in}$) at 100 $R_{\rm g}$ (as suggested by the long-term evolution of the diskbb parameters; Fig. 2), and the emissivity indices (q_1 and q_2) at 3, with the reflection fraction fixed at -1 so that relxill accounts only for the reflected component. This model provided a good fit with χ^2/d.o.f. = 1853/1662, with the best-fit parameters listed in Table D.2, yielding a cutoff energy of 217^{+72}_{-50} keV and an inclination angle of 58^{+16}_{-31} °.

Appendix C: Long-term light-curve modeling and binary constraints

C.1. FRED modeling

We fit the multi-instrument long-term X-ray light curve, excluding the pre-outburst upper limits, using a modified FRED model (Powell et al. 2007) parameterized as

$$F(t) = \begin{cases} A \exp[(t - t_{\rm p})/\tau_{\rm r}], & t < t_{\rm p}, \\ (A - F_d) \exp[-(t - t_{\rm p})/\tau_{\rm d}] + F_d, & t \geq t_{\rm p}, \end{cases} \quad \text{(C.1)}$$

where A, F_d, $t_{\rm p}$, $\tau_{\rm r}$, and $\tau_{\rm d}$ denote the peak flux, the late-time constant flux level, the time of the flux peak relative to the initial EP/WXT detection, and the rise and decay timescales, respectively. The best-fit parameters are $A = (4.75 \pm 0.08) \times 10^{-10}$ erg cm^{-2} s^{-1}, $F_d = (0.68 \pm 0.02) \times 10^{-10}$ erg cm^{-2} s^{-1}, $t_{\rm p} = 2.6 \pm 0.2$ days, $\tau_{\rm r} = 2.5^{+0.5}_{-0.4}$ days, and $\tau_{\rm d} = 15.7^{+0.5}_{-0.7}$ days.

We note that the EP/WXT flux measurements appear systematically offset from those obtained with other telescopes during the decay phase, likely due to the narrower energy band of EP/WXT.

C.2. Binary system parameters

Assuming a 10 $M_\odot$ BH accretor and adopting a viscosity parameter of $\nu = 10^{15}\,\mathrm{cm^2\,s^{-1}}$ (Powell et al. 2007), the outer disk radius can be estimated from the exponential decay timescale as

$$R_{\rm disc}(\tau_d) = \sqrt{3\nu\tau_d} \approx 6\times10^{10}\,\mathrm{cm} \approx 4\times10^{4}\,R_g. \tag{C.2}$$

Assuming that this radius is comparable to the circularization radius $R_{\rm circ}$ and a binary mass ratio of $q = 0.1$, the orbital period can be estimated using Eq. 4.18 of Frank et al. (1992):

$$P_{\rm orb} = \frac{2\pi R_\odot^{3/2}}{\sqrt{GM_\odot}}\left(\frac{M_1}{M_\odot}\right)^{-1/2} \times\left(\frac{R_{\rm circ}}{R_\odot}\right)^{3/2}(1+q)^{-2}\left[0.500 - 0.227\log_{10} q\right]^{-6}. \tag{C.3}$$

This gives an estimated orbital period of $P_{\rm orb} \approx 4.3$ hr. However, due to observational gaps caused by Sun-avoidance constraints, we cannot exclude the possibility that the source experienced a reflare between 2025 October and 2026 March, which could introduce uncertainties into the system parameter estimations.

Appendix D: Supplementary figures and tables

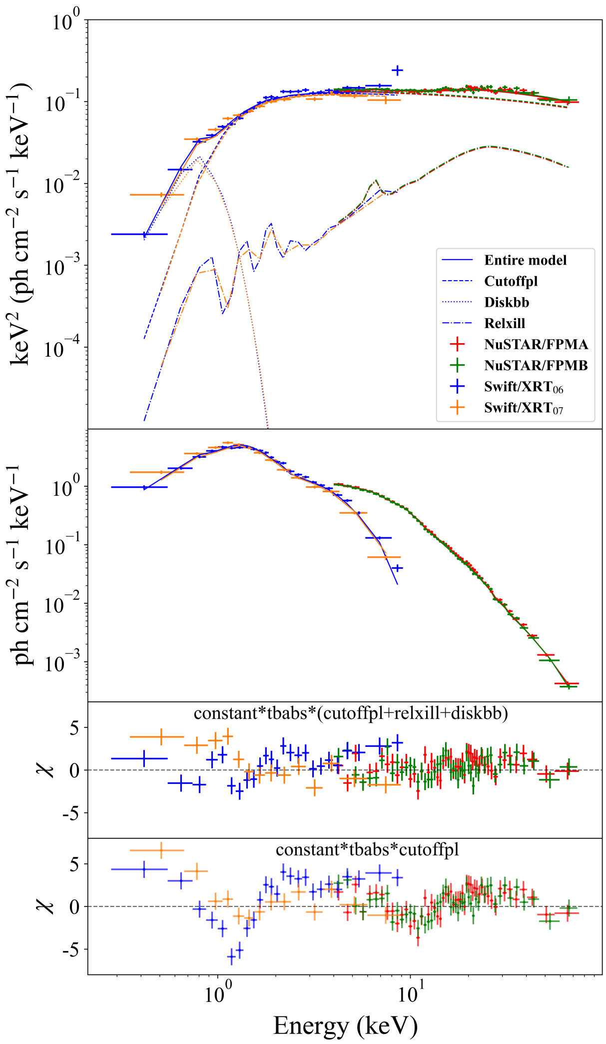

Fig. D.1. Joint spectral fitting of the *Swift*/XRT (2025 September 23 and 26) and *NuSTAR* (2025 September 24) observations. Top: Unfolded spectrum in units of keV^2 (ph cm^{-2} s^{-1} keV^{-1}) with the best-fit model tbabs*(cutoffpl+relxill+diskbb). Second: Unfolded spectrum in units of ph cm^{-2} s^{-1} keV^{-1}. Third and bottom: Residuals for tbabs*(cutoffpl+relxill+diskbb) and tbabs*cutoffpl, respectively. The spectra are re-binned for display purposes.

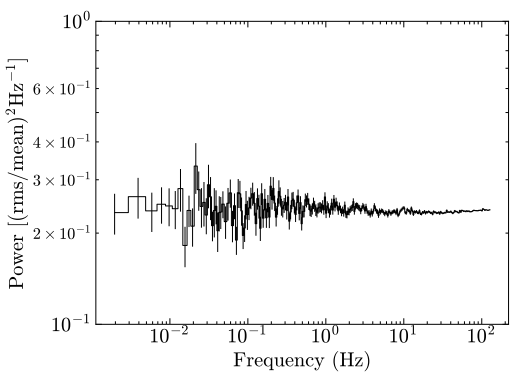

Fig. D.2. Averaged power density spectrum of the *NuSTAR* observation on 2025 September 24 in the 4–78 keV energy band.

Table D.1. X-ray follow-up observations.

Start Time (UTC)	Instrument	Mode	ObsID	Exposure Time (s)
2025-09-17T08:57:58.87	SVOM/MXT	...	1140857003	7074
2025-09-17T11:34:24.89	EP/FXT	FXT-A: FF; FXT-B: PW	08500000408	3127
2025-09-17T21:38:40.10	*Swift*/XRT	PC	03000100001	1254
2025-09-17T23:14:02.46	*Swift*/XRT	WT	03000100002	1849
2025-09-18T14:04:33.83	SVOM/MXT	...	1140857021	4727
2025-09-19T06:14:55.31	SVOM/MXT	...	1140857023	6559
2025-09-19T15:36:09.57	*Swift*/XRT	WT	03000100003	998
2025-09-20T06:30:28.03	SVOM/MXT	...	1140857026	11846
2025-09-20T10:27:26.40	*Swift*/XRT	WT	03000100004	1638
2025-09-21T06:46:03.71	SVOM/MXT	...	1140857027	11855
2025-09-22T15:15:57.36	*Swift*/XRT	WT	03000100005	784
2025-09-23T09:45:06.00	*Swift*/XRT	WT	03000100006	1075
2025-09-24T11:26:09.00	*NuSTAR*	...	91101336002	20706
2025-09-26T21:38:24.43	*Swift*/XRT	WT	03000100007	518
2025-10-01T02:42:43.38	*Swift*/XRT	WT	03000100008	1185
2025-10-02T04:58:48.06	*Swift*/XRT	WT	03000100009	853
2025-10-03T07:22:02.96	*Swift*/XRT	WT	03000100011	942
2025-10-04T02:03:26.87	*Swift*/XRT	PC	03000100010	632
2025-10-05T23:05:37.37	*Swift*/XRT	PC	03000100012	862
2025-10-06T00:51:56.20	*Swift*/XRT	WT	03000100013	907
2025-10-07T04:32:07.57	*Swift*/XRT	WT	03000100014	716
2025-10-08T00:47:33.13	*Swift*/XRT	PC	03000100015	867
2025-10-11T00:04:24.96	*Swift*/XRT	PC	03000100016	732
2025-10-14T01:17:35.47	*Swift*/XRT	PC	03000100017	924
2025-10-17T06:38:09.47	*Swift*/XRT	PC	03000100019	764
2025-10-18T09:00:13.33	*Swift*/XRT	PC	03000100018	824
2025-10-23T16:22:59.63	*Swift*/XRT	PC	03000100021	839
2025-11-01T06:33:13.37	*Swift*/XRT	PC	03000100022	827
2026-04-22T19:05:30.83	EP/FXT	FXT-A: FF; FXT-B: PW	11900697344	3659

Table D.2. Best-fitting spectral parameters of the joint *Swift*/XRT and *NuSTAR* spectra.

Component	Parameter	Value
Constant	factor (FPMA)	1 (frozen)
	factor (FPMB)	1.024 ± 0.007
	factor (XRT_{06})	$0.95^{+0.02}_{-0.03}$
	factor (XRT_{07})	0.91 ± 0.03
TBabs	N_H (10^{22} cm^{-2})	0.90 ± 0.05
Cutoffpl	Γ	$2.08^{+0.02}_{-0.03}$
	E_{cut} (keV)	217^{+72}_{-50}
	norm (photons/keV/cm^2)	$0.157^{+0.004}_{-0.007}$
Relxill	q_1	3 (frozen)
	q_2	3 (frozen)
	R_{br} (R_g)	1000 (frozen)
	a	0.998 (frozen)
	Inclination (°)	58^{+16}_{-31}
	R_{in} (R_g)	100 (frozen)
	R_{out} (R_g)	1000 (frozen)
	z	0 (frozen)
	Γ	$= \Gamma_{cutoffpl}$
	$\log\xi$	$1.70^{+0.09}_{-0.35}$
	A_{Fe}	< 0.6
	E_{cut} (keV)	$= E_{cutoffpl}$
	Reflection fraction	-1 (frozen)
	norm (10^{-4})	$2.1^{+0.6}_{-1.0}$
Diskbb	T_{in} (keV)	0.083 ± 0.004
	norm (10^7) [$(R_{in}/D_{10})^2 \cos\theta$]	$3.1^{+1.9}_{-1.5}$
	χ^2/d.o.f	1853/1662

Notes. The spectra are jointly fitted with the model constant*tbabs*(cutoffpl+relxill+diskbb). Errors are given at the 90% confidence level. XRT_{06} and XRT_{07} correspond to *Swift*/XRT ObsIDs 03000100006 and 03000100007.

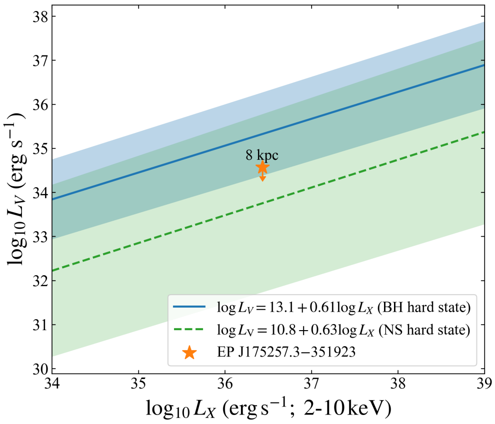

Fig. D.3. Optical/X-ray luminosity relation for LMXBs. The blue line and shaded region show the empirical correlation and its 1σ uncertainty for hard-state BH XRBs, while the green line and shaded region show those for hard-state NS XRBs (Russell et al. 2006). The star symbol marks EP J175257.3–351923 at an assumed distance of 8 kpc, with a de-reddened V-band luminosity near the outburst peak of $\lesssim 4 \times 10^{34}$ erg s^{-1} and a quasi-simultaneous 2–10 keV X-ray luminosity of $\sim 3 \times 10^{36}$ erg s^{-1}.

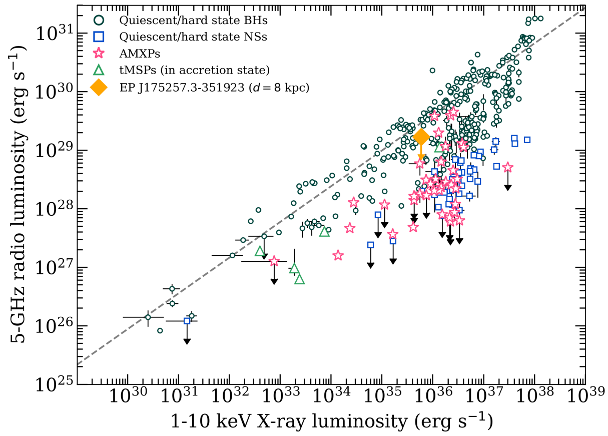

Fig. D.4. Radio versus X-ray luminosities of LMXBs in the hard state (adapted from Bahramian & Rushton 2022), with EP J175257.3–351923 overlaid. The radio constraint is a 3σ VLASS upper limit at 3 GHz (2026 February 1), converted to 5 GHz assuming a flat radio spectrum. The X-ray luminosity is from the EP/FXT observation on 2026 April 22. Although the X-ray and radio observations are not simultaneous, the source had entered a plateau phase, and the X-ray luminosity is therefore assumed to be comparable at the VLASS epoch. Both luminosities assume a distance of 8 kpc.